ChemComm

COMMUNICATION

View Article Online
View Journal | View Issue

Cite this: *Chem. Commun.*, 2025, **61**, 278

Received 16th October 2024,
Accepted 25th November 2024

DOI: 10.1039/d4cc05466k

rsc.li/chemcomm

Self-supported Ni/NiO heterostructures with a controlled reduction protocol for enhanced industrial alkaline hydrogen evolution†

Haiyang Wang,[a] Cong Chen,*[a] Junxia Shen,[a] Pierre-Yves Olu,[b] Longhui Li,[c] Wen Dong,[a] Ronglei Fan *[a] and Mingrong Shen *[a]

Self-supported Ni/NiO heterostructures with controllable ratios used in industrial alkaline water electrolysis (AWE) systems lead to an ultralow voltage of 1.79 V at 400 mA cm^{-2} for 2 weeks, ascribed to the synergic combination of abundant active sites, rapid electron/mass transfer and optimal HER kinetics.

Hydrogen production by alkaline water electrolysis (AWE) has attracted extensive attention in both academic research and industrial applications on account of its high technological maturity, low cost, and long lifespan.[1] Further large-scale development of this technology hinges on the exploration of inexpensive, efficient and stable electrocatalysts for the sluggish hydrogen evolution reaction (HER).[2] With excellent alkali corrosion resistance and high electrical conductivity, metallic Ni represented by RANEY® Ni derived from Ni–Al alloy has been widely used as the HER catalyst in industrial AWE equipment. Nevertheless, bare metallic nickel still suffers from sluggish HER kinetics because of the shortage of effective sites for water dissociation in the Volmer step and the excessive hydrogen adsorption in the Heyrovsky/Tafel step.[3,4] Considering that Ni oxides (NiO) can greatly facilitate the Volmer step by promoting the cleavage of HO–H bonds,[5] designing a Ni/NiO heterostructure with a controllable ratio of Ni and NiO is a relevant strategy to improve alkaline HER activity. For example, Wan and colleagues reported a thermal annealing synthesis in order to optimize the Ni and NiO synergy in Ni/NiO nanocrystals by regulating their sizes, which led to improved alkaline HER activity.[6] Cui *et al.* proposed a self-assembly process combined with a calcination process to synthesize carbon onion-coated Ni/NiO nanoparticles. They found that regulating the ratio of Ni/NiO in the composites by controlling the calcination temperature could effectively promote the HER performance in alkaline conditions.[2] Recently, Han and co-workers reported a controlled oxidation protocol to form an *in situ* thin NiO surface layer onto the metallic Ni, which demonstrated progressive enhanced intrinsic catalytic activity toward the HER.[7] Although some progress has been made, in most cases, additional binders and additives are required to boost the adhesion of electrocatalyst nanoparticles on the conducting substrates, which may severely limit their long-term stability.[8] Furthermore, most fabrication methods employed high temperature annealing treatments with multiple reaction steps, which are usually complex, and time- and energy-consuming.[9] Therefore, it remains a challenge to fabricate self-supported Ni/NiO with controllable ratios for high HER performance in a facile and scalable way.

Herein, we proposed a facile laser ablation process, followed by a chemical reduction treatment in $NaBH_4$ aqueous solution, to directly grow self-supported Ni/NiO heterostructures with controllable ratios on the Ni mesh (NM) substrate (denoted as RL-NM). By adjusting the conditions of chemical reduction treatment, we found that the ratio of Ni/NiO in the heterostructures was a key factor in determining the alkaline HER activity of the RL-NM electrode. Notably, the optimized RL-NM shows excellent HER activity with a low overpotential of 264 mV to achieve 100 mA cm^{-2}, along with a stable operation for 2 weeks at 400 mA cm^{-2} under industrial AWE configurations (30 wt% KOH, 80 °C), much superior to RANEY® Ni under identical conditions.

In this study, NM is selected as the substrate, owing to its good mechanical strength and conductivity. The schematic illustration of RL-NM synthesis is shown in Fig. 1a. First, the NM was ablated using a high energy laser, referred to as L-NM. Then, RL-NM was obtained by chemical reduction treatment of L-NM in 0.5 M $NaBH_4$ for different durations, denoted as R_xL-NM (x represents the time of chemical reduction treatment). The detailed experimental process can be found in the ESI† (see the ESI†). After

[a] *School of Physical Science and Technology, Jiangsu Key Laboratory of Frontier Material Physics and Devices, Collaborative Innovation Center of Suzhou Nano Science and Technology, Soochow University, 1 Shizi Street, Suzhou 215006, China. E-mail: cchen96@suda.edu.cn, rlfan@suda.edu.cn, mrshen@suda.edu.cn*
[b] *John Cockerill Hydrogen S.A, 1 Rue Jean Potier, 4100 Seraing, Belgium*
[c] *Zhejiang Jiafeili New Material Co, Ltd, No. P (2022)06 Longpan Mountain Block, Yunfeng Street Industrial Park, Lishui 323301, China*

† Electronic supplementary information (ESI) available. See DOI: https://doi.org/10.1039/d4cc05466k

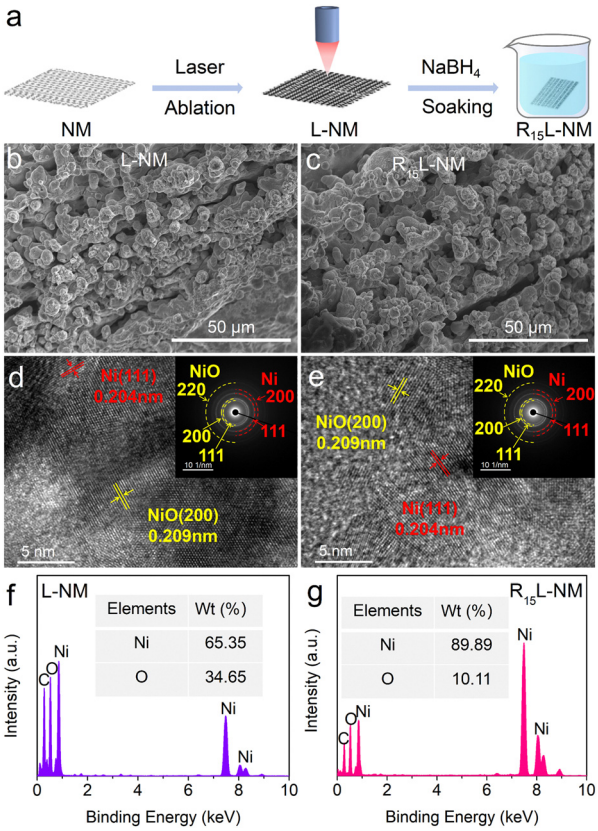

Fig. 1 (a) Schematic illustration of R_{15}L-NM. (b) and (c) SEM images of L-NM and R_{15}L-NM. (d) and (e) STEM-EDX mapping of L-NM and R_{15}L-NM. (f) and (g) EDX spectra of L-NM and R_{15}L-NM.

laser ablation, the NM turned to black color (Fig. S1, ESI†), while there was no visible change in the electron microscope (SEM) image in Fig. 1b, and L-NM displays a rough morphology composed of sharp arrays and particles compared to the smooth morphology of bare NM (Fig. S2, ESI†). After $NaBH_4$ treatment for 15 min, there is no obvious change in the surface morphology of R_{15}L-NM (Fig. 1c). The SEM images of R_xL-NM processed at other times are shown in Fig. S3 (ESI†). These results indicate that chemical reduction treatment does not significantly alter the surface morphology of the electrode. Obviously, this rough surface structure can expose more active sites and accelerate charge/mass transfer.[10,11] To further reveal the microscopic morphology, transmission electron microscopy (TEM) was conducted. For L-NM and R_{15}L-NM, the clear lattice fringes of 0.204 and 0.209 nm belong to the Ni (111) and NiO (200) planes, respectively. The coexistence of lattice planes of Ni and NiO can also be observed in the selected area electron diffraction (SAED) images (Fig. 1d and e).[7] The emergent NiO species appear, indicating that the NM was oxidized. The effect of $NaBH_4$ treatment is unveiled by scanning transmission electron microscopy (STEM) combined with energy dispersive X-ray (EDX) spectra. To eliminate the influence of air or moisture, all samples were etched for 5 nm *via* Ar^+ treatment before the test. As shown in Fig. 1f and g, the actual content of Ni and O is 65.35 and 34.65 wt% for L-NM. After chemical reduction for 15 min, the Ni : O ratio increases to 89.89 : 10.11 wt%. The EDX spectra of other samples treated in $NaBH_4$ solution for different times are also shown in Fig. S4 (ESI†). Furthermore, the cross-sectional SEM image and EDX mapping images of R_{15}L-NM clearly show the interface between the Ni/NiO heterostructure and NM substrate (Fig. S5, ESI†). These results indicate that self-supported porous Ni/NiO heterostructures with different Ni : NiO ratio have been successfully prepared by laser ablation and chemical reduction methods, which could endow more active sites and optimized kinetics for the HER.

The structural information of different samples was further studied by X-ray diffraction (XRD) and Raman spectroscopy. For better comparison, the NiO/L-NM electrode obtained by annealing L-NM in an air atmosphere was used as the control sample. As indicated in Fig. 2a, besides the three diffraction peaks of metallic Ni, the XRD pattern depicts obvious peaks at $2\theta = 37.3$, 43.3 and 62.9°, matching well with the (111), (200) and (220) of NiO.[12,13] However, the intensity of the diffraction peaks of NiO follows this order with the increase of the reduction time in $NaBH_4$: R_5L-NM > R_{10}L-NM > R_{15}L-NM > R_{30}L-NM (Fig. S6, ESI†). The surface composition changes were further corroborated by Raman spectroscopy (Fig. 2b). A broad Raman peak at ~524 cm^{-1} appears, which can be assigned to the Ni–O band.[14] During the controlled chemical reduction process, the Raman peak of Ni–O gradually weakens, indicating that the ratio of NiO species decreases with the increase of the reduction time. The surface valence state is analysed by X-ray photoelectron

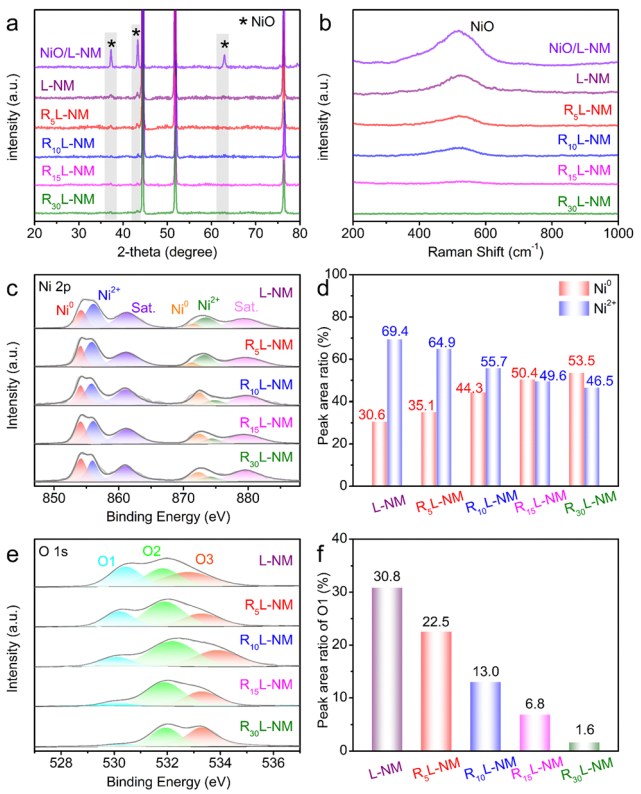

Fig. 2 Spectrometric characteristics of various samples. (a) XRD patterns, (b) Raman spectra, (c) high-resolution XPS spectra of Ni 2p and (d) corresponding proportion of Ni^0 and Ni^{2+}, (e) high-resolution XPS spectra of O 1s and (f) corresponding proportion of M–O.

spectroscopy (XPS) in Fig. 2c. For L-NM, the Ni 2p orbital peaks at 854.2 and 871.5 eV can be assigned to the Ni^0, and the peaks at 856 and 873.5 eV can be assigned to Ni^{2+}, following assignments of previous reports.[7,15] The dominant existence of Ni^{2+} indicates that a large portion of Ni species were oxidized to NiO during the laser ablation process. After the chemical reduction process, the quantitative ratio of Ni^{0+} increases while the ratio of Ni^{2+} decreases gradually as the time increases (Fig. 2d and Table S1, ESI†). The O 1s peak was fitted to three feature peaks, which were linked to metal–oxygen (M–O), metal hydroxide (M–OH) and adsorbed water at ~529.6, 531.5 and 533.2 eV, respectively.[16] Compared to L-NM, the proportion of M–O in RL-NM decreases from 30.8 to 1.6 with the increase of the reduction time (Fig. 2e and f). Considering XRD, Raman and XPS measurements, we conclude that an adjustable ratio of Ni/NiO can be achieved in RL-NM by chemical reduction.

The HER performance of different samples was firstly evaluated using a three-electrode system. For the L-NM samples, as the chemical reduction time increases from 0 to 15 min, the overpotential at -10 mA cm^{-2} gradually decreases while the Ni/NiO ratio increases from 0.44 to 1.01. Further increase in the chemical reduction time will lead to increases in both overpotential and Ni/NiO ratio (Fig. S7, ESI†). The RL-NM electrode with the optimal chemical reduction duration of 15 min displays the best HER activity in both laboratory (1 M KOH, 25 °C) and industrial conditions (30 wt% KOH, 80 °C), which should be due to the optimal balance between the Ni and NiO components in the Ni/NiO heterostructures that synergistically facilitate both reaction steps for enhanced alkaline HER activity, which was further supported by theoretical calculations (Fig. S8–S11, ESI†). This sample is referred to as RL-NM, unless otherwise specified. Furthermore, all the above electrodes show nearly 100% Faraday efficiency for the HER and high stability for 120 h, demonstrating huge potential of industrial application (Fig. S12 and Table S2, ESI†). As shown in Fig. 3a, the overpotentials for RL-NM at the current densities of 10, 100 and 1000 mA cm^{-2} are 166, 264 and 395 mV, which overmatches the control samples and other recently reported alkaline HER catalysts (Table S3, ESI†). Tafel slopes derived from LSV curves bring deeper understanding to the HER kinetics. In Fig. 3b, RL-NM exhibits a low Tafel slope of 70.8 mV dec^{-1}, which is significantly lower than that of NiO/L-NM (143.9 mV dec^{-1}), NM (139.4 mV dec^{-1}), RANEY® Ni (123.4 mV dec^{-1}) and L-NM (114.6 mV dec^{-1}), indicating that adjustment of the ratio of Ni and NiO in the NiO/Ni heterostructures can keep the balance between water dissociation in the Volmer step and hydrogen adsorption in the Heyrovsky/Tafel step,[6] thus improving the HER activity. In addition, the turnover frequence (TOF) of various electrodes was calculated at -300 mV. As displayed in Fig. 3c, the RL-NM indicates the best TOF value up to 0.87 s^{-1}, indicating its superb intrinsic catalytic activity. To gain deeper insights into the activity of RL-NM, electrochemical impedance spectroscopy (EIS) was performed. The Nyquist plots were fitted by an equivalent circuit model (Fig. S13, ESI†). The RL-NM catalyst bears a relatively low charge transfer resistance, indicating its rapid interfacial charge transfer kinetics (Fig. 3d and Table S4 ESI†). Besides, the electrochemical double-layer capacitances (C_{dl})

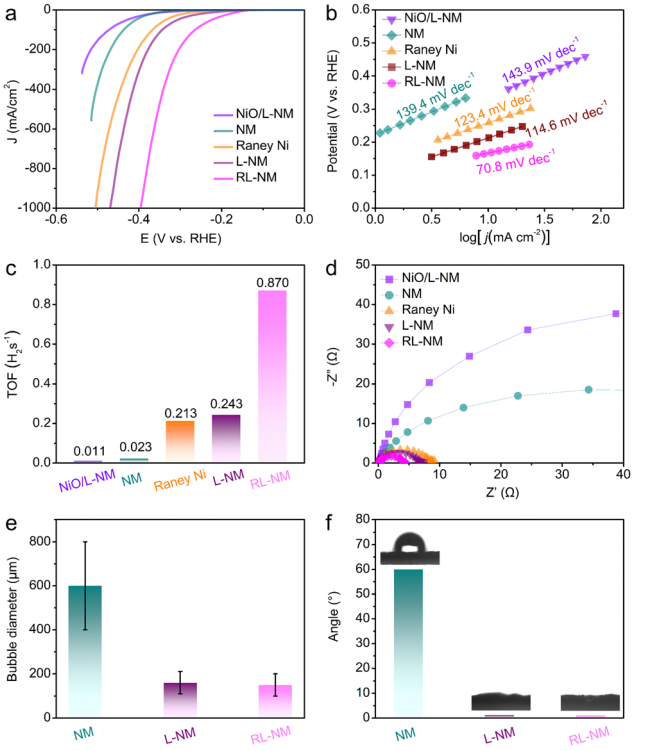

Fig. 3 HER performance of NiO/L-NM, NM, RANEY® Ni, L-NM and RL-NM electrodes under industrial AWE conditions. (a) iR corrected LSV curves, (b) Tafel plots, (c) TOF values, and (d) Nyquist plots. (e) Average diameter and (f) water contact angle for NM, L-NM and RL-NM electrodes.

of the electrodes were measured by cyclic voltammetry to calculate the electrochemically active surface areas (ECSAs).[17] Notably, the L-NM exhibits higher C_{dl} and ECSAs values of 6.98 mF cm^{-2} and 174.5, which far surpass NM (0.73 mF cm^{-2} and 18.25) (Fig. S14 and S15, ESI†). This could be ascribed to improved surface roughness after laser ablation, as is proved in SEM. However, the C_{dl} and ECSA values are relatively similar for NiO/L-NM, L-NM and RL-NM, which is explained by unsignificant morphological changes after the thermal process or after the reduction treatment. In order to further understand the intrinsic activity, the LSV curves were normalized to their ECSA. The RL-NM catalyst displays significantly higher intrinsic activity than other control samples due to its optimal ratio of Ni and NiO in the Ni/NiO heterostructures (Fig. S16, ESI†). In addition, rough morphology could endow the catalysts with hydrophilic and aerophobic properties, thus accelerating mass transfer and increasing the number of active sites.[18,19] The generation and release of bubbles, as well as the bubble contact angles were recorded using a digital camera setup. As indicated in Fig. 3e and Fig. S17, ESI,† for L-NM and RL-NM, the size and number of as-formed bubbles are obviously smaller than pure NM (159 and 144 μm *vs.* 599 μm, respectively), revealing a weakened adhesion of bubbles during the HER for laser ablated surfaces at large current density. Furthermore, L-NM and RL-NM have a water contact angle close to zero degrees, compared to NM with 59.7°. The enhanced hydrophilicity of laser ablated surfaces enables the permeation of electrolyte, thus facilitating the HER and ensuring that the HER can occur with less mass-transfer limitation.

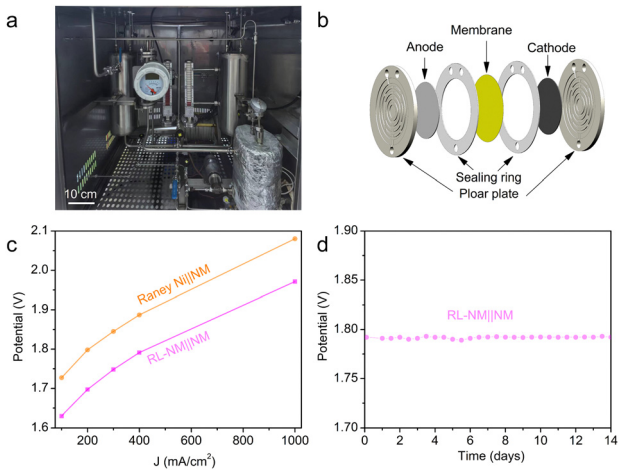

Fig. 4 (a) Photo of industrial AWE configuration, and (b) schematic diagram of the industrial electrolyzer. (c) Comparison of activity between RL-NM‖NM and RANEY® Ni‖NM at different current densities. (d) Durability test for the RL-NM‖NM electrolyzer.

Building on the superior HER activity and stability of RL-NM under both laboratory and industrial conditions, the practical AWE performance was investigated in the industrial configuration by assembling the RL-NM and NM as the cathode and anode (called as RL-NM‖NM), respectively, as shown in Fig. 4a. The industrial alkaline electrolyzer consists of a bipolar plate, catalytic electrodes, sealing rings and porous membrane (Fig. 4b). For comparison, commercial RANEY® Ni electrode and NM also as a cathode and anode (called as RANEY® Ni‖NM) were equipped in this electrolyzer. Impressively, compared to RANEY® Ni‖NM, the RL-NM‖NM electrolyzer displays superior activity at different current densities (1.97 *vs.* 2.08 V at 1 A cm^{-2}), as displayed in Fig. 4c. Furthermore, RL-NM‖NM cells lead to a higher energy efficiency (82.6%), compared to RANEY® Ni‖NM (78.4%), and the detailed calculation process can be found in the ESI.† Moreover, RL-NM‖NM shows a promising durability with stable performances for two weeks of operation (Fig. 4d). Postmortem analysis of the electrodes after durability testing shows no visible morphological change for RL-NM (Fig. S18, ESI†). In addition, the XRD, Raman and XPS analyses reveal that the chemical composition of RL-NM has negligible changes after the stability test (Fig. S19, ESI†). Moreover, the RL-NM electrode also displays superior activity under anion exchange membrane (AEM) conditions (Fig. S20, ESI†). These results further showcase that the as-prepared RL-NM has an appealing potential for industrial application.

In summary, we adopted a novel strategy to prepare self-supported Ni/NiO heterostructures with a controllable Ni : NiO ratio, aimed at enhancing the HER activity due to a synergetic effect between Ni and NiO. Besides, controlled NiO/Ni heterostructures with rough morphology enable abundant density of active sites for the HER, as well as accelerate the electron and mass transfer processes. Consequently, the RL-NM features a low overpotential of 264 mV at 100 mA cm^{-2} and Tafel slope of 70.8 mV dec^{-1} under industrial conditions. When assembled with NM for overall water splitting in industrial AWE conditions, RL-NM‖NM shows a low voltage of 1.97 V at 1 A cm^{-2}, stable for at least 2 weeks at 400 mA cm^{-2}, surpassing the performance of a commercial RANEY® Ni‖NM electrolyzer (2.08 V). This work provides an appealing pathway for developing industrial scale highly efficient HER catalysts for hydrogen production.

This work was supported by the National Natural Science Foundation of China (Grant No. 52002259, 52372216, and 52272228), and a key project of carbon peak carbon neutralization technology support from Suzhou Science and Technology Bureau (Grant No. ST202227).

Data availability

The data supporting this article have been included as part of the ESI.†

Conflicts of interest

There are no conflicts to declare.

Notes and references

1 M. N. Lakhan, A. Hanan, A. Hussain, I. Ali Soomro, Y. Wang, M. Ahmed, U. Aftab, H. Sun and H. Arandiyan, *Chem. Commun.*, 2024, **60**, 5104–5135.
2 S. Marimuthu, A. Shankar and G. Maduraiveeran, *Chem. Commun.*, 2023, **59**, 2600–2603.
3 H. Sun, B. Yao, Y. Han, L. Yang, Y. Zhao, S. Wang, C. Zhong, J. Chen, C. P. Li and M. Du, *Adv. Energy Mater.*, 2024, 2303563.
4 Y. Yan, Q. Ma, F. Cui, J. Zhang and T. Cui, *Electrochim. Acta*, 2022, **430**, 141090.
5 C. Li, J.-Y. Xue, W. Zhang, F.-L. Li, H. Gu, P. Braunstein and J.-P. Lang, *Nano Res.*, 2022, **16**, 4742–4750.
6 L. Zhao, Y. Zhang, Z. Zhao, Q. H. Zhang, L. B. Huang, L. Gu, G. Lu, J. S. Hu and L. J. Wan, *Natl. Sci. Rev.*, 2020, **7**, 27–36.
7 L. Qiao, C. Xi, C. Li, K. Zhang, Q. Li, J. Han and Y. Ding, *Adv. Funct. Mater.*, 2024, 2402286.
8 C. I. Bernäcker, T. Gimpel, A. Bomm, T. Rauscher, S. Mauermann, M. Li, E. G. Hübner, W. Schade and L. Röntzsch, *J. Power Sources*, 2022, 538.
9 G. Ou, P. Fan, H. Zhang, K. Huang, C. Yang, W. Yu, H. Wei, M. Zhong, H. Wu and Y. Li, *Nano Energy*, 2017, **35**, 207–214.
10 C. Chen, J. Zhou, J. Shen, T. An, Z. Wei, Y. Zhang, S. Ju, Y. Peng, R. Fan and M. Shen, *Chem. Eng. J.*, 2024, **484**, 149456.
11 Q. Ren, L. Feng, C. Ye, X. Xue, D. Lin, S. Eisenberg, T. Kou, E. B. Duoss, C. Zhu and Y. Li, *Adv. Energy Mater.*, 2023, 2302073.
12 T. Zhang, M.-Y. Wu, D.-Y. Yan, J. Mao, H. Liu, W.-B. Hu, X.-W. Du, T. Ling and S.-Z. Qiao, *Nano Energy*, 2018, **43**, 103–109.
13 T. An, Q. Jin, J. Shen, W. Zhang, Q. Huang, C. Chen, W. Dong, R. Fan and M. Shen, *Int. J. Hydrogen Energy*, 2024, **64**, 282–289.
14 Z. Wu, Z. Zou, J. Huang and F. Gao, *J. Catal.*, 2018, **358**, 243–252.
15 A. Y. Faid, A. O. Barnett, F. Seland and S. Sunde, *Electrochim. Acta*, 2020, **361**, 137040.
16 X. Jiang, V. Kyriakou, C. Song, X. Wang, S. Costil, C. Deng, T. Liu, T. Jiang and H. Liao, *J. Energy Chem.*, 2024, **93**, 511–518.
17 R. Balaji, T. T. Nguyen, Q. P. Ngo, N. H. Kim and J. H. Lee, *Adv. Funct. Mater.*, 2024, 2410672.
18 X. Cao, R. Fan, J. Zhou, C. Chen, S. Xu, S. Zou, W. Dong, X. Su, S. Ju and M. Shen, *Chem. Commun.*, 2022, **58**, 1569–1572.
19 Z. Zhu, Y. Lin, P. Fang, M. Wang, M. Zhu, X. Zhang, J. Liu, J. Hu and X. Xu, *Adv. Mater.*, 2023, 2307035.